RSC Applied Interfaces

ROYAL SOCIETY OF CHEMISTRY

PAPER

View Article Online
View Journal | View Issue

Cite this: *RSC Appl. Interfaces*, 2026, 3, 376

Edge *vs.* basal plane of $Ti_3C_2T_x$ MXene: enhanced inherent electrochemistry, electron transfer, and catalytic activity at the edge

Shubham B. Upadhye, [a] Gopal K. Pradhan[b] and Pranati Nayak *[a]

The electrochemistry at the edge and basal plane of two-dimensional (2D) layered materials has been of immense interest recently. While significant advances have been made in this direction for layered graphite, graphene, transition metal dichalcogenides (TMDs), and monoelemental black phosphorus, understanding the fundamental differences in the electrochemical behavior of 2D $Ti_3C_2T_x$ MXene edges compared to the basal plane remains elusive. This work employs a simple and scalable fabrication technique to fabricate edge and basal plane $Ti_3C_2T_x$ MXene electrodes and to explore their fundamental electrochemical and electrocatalytic properties. Compared to the basal plane, the innate oxidation of MXene is found to be significantly higher at the edge plane electrodes, with a limited working potential window for a series of electrolytes. The heterogeneous electron transfer rate for the edge is found to be ~3.3-fold higher than the basal plane for common redox mediators such as ferrocyanide $[Fe(CN)_6]^{3-}$, and hexaammineruthenium $[Ru(NH_3)_6]^{3+}$, respectively. In addition, the preferentially exposed edge sites offer low potential detection of biomarkers and significantly improved catalytic activity for H_2 evolution. This work elucidates how exposed edge sites can dramatically impact the innate electrochemical properties, enabling new opportunities for catalysis and other electrochemical applications.

Received 11th November 2025,
Accepted 5th January 2026

DOI: 10.1039/d5lf00354g

rsc.li/RSCApplInter

Introduction

The innate electrochemistry (electrochemistry of the material when used as an electrode), charge transfer kinetics, and catalytic activity of 2D materials have long been a subject of extensive debate due to their structural anisotropy, leading to distinct properties at edge plane sites compared to the basal plane.[1,2] The basal plane sites of 2D sheets are often of low defect density, atomically flat, and inert. In contrast, the edge plane features dangling bonds and abundant defect sites due to abrupt lattice termination and unsaturated coordination.[3,4] As the range of operational potential windows depends on the proclivity of individual atoms toward innate redox reactions, understanding the instinctive response of atoms in the basal plane or edge is indispensable for their operational use in electrochemical devices. For example, pristine graphene exhibits no innate electrochemistry over a wide potential window, enabling its viability for a range of potential applications, including catalysis, energy production, storage, and sensing.[5–7] However, compared to the inert basal plane, graphene edges often contain more electro-reducible inherent oxygen groups, which, upon elimination, lead to higher catalytic activity at the edge.[1] Similarly, the heterogeneous electron transfer rates at the edge of the graphene monolayer for molecular probes like $[Fe(CN)_6]^{3-/4-}$, $[Ru(NH)_3]^{3+/2+}$ are seen to be rapid compared to the basal plane.[8] Additionally, the graphene edge has shown higher oxygen reduction reactions (ORR) and hydrogen evolution reactions (HER) activities compared to the basal planes.[9]

2D materials other than graphene, such as TMDs, layered pnictogens, metal oxides, layered double hydroxides (LDHs), hexagonal boron nitride (h-BN), and graphitic carbon nitride (g-C_3N_4), are equipped with varying exotic properties favorable for potential electrochemical applications.[10] Akin to graphene, g-C_3N_4 exhibits a broad operational window and negligible inherent electroactivity and catalytic effect due to the lack of electroactive surface functional groups in its pristine form.[11] However, the heterogeneous charge transfer rate is comparable to that of the graphene basal plane. In contrast to graphene and g-C_3N_4, transition metal dichalcogenides (TMDs) exhibit inherently irreversible redox behavior stemming from the redox behavior of the chalcogens, particularly for disulfides (*e.g.*, MoS_2, WS_2) and diselenides ($MoSe_2$, WSe_2), which markedly narrows down the working electrochemical potential window.[12–14] Also, the basal plane is found to be extensively inert, showing almost no innate electrochemistry, a slow heterogeneous electron

[a] *Department of Engineering and Materials Physics, Institute of Chemical Technology-Indian Oil Odisha Campus, Bhubaneswar 751013, India. E-mail: p.nayak@iocb.ictmumbai.edu.in*
[b] *Department of Physics, School of Applied Science, KIIT Deemed to be University, Bhubaneswar, 751024, India*

transfer (HET) rate, and HER activities compared to the edge planes.[2,15–19] The edge plane for MoS_2 exhibits a much larger HET rate constant k_0 of 4.96×10^{-5} and 1.1×10^{-3} cm s^{-1} for both inner $[Ru(NH_3)_6]^{3+/2+}$ and outer sphere redox probes $[Fe(CN)_6]^{3-/4-}$ cm s^{-1}, respectively, compared to the basal plane.[15] The exposed edges are found to be markedly catalytic compared to the basal plane for many catalytic electrochemical reactions (*e.g.*, HER, oxygen evolution reaction-OER, ORR, CO_2 reduction reactions) and sensing. Unlike the diselenide or disulfides, the inherent electrochemistry of ditellurides displays distinct features stemming from the tellurium redox electrochemistry, resulting in the formation of TeO_2.[20] A similar trend is observed for the layered pnictogen family (P, As, Sb, Bi), which is inherently prone to self-oxidation (*e.g.*, P(0) to P(v) state).[21] In addition, the passivated surface oxides noticeably narrow their working potential window.[22] Also, the innate properties are shown to be highly influenced by surface anisotropy, exemplified by the higher HET rate activity of edges compared to basal planes. Likewise, the electrocatalytic activity is manifested faster at the edges compared to the basal planes for HER and ascorbic acid oxidation.[23]

Since the successful synthesis of 2D $Ti_3C_2T_x$ in 2011, a new class of two-dimensional materials known as MXenes has drawn significant scientific attention over the past decade.[24] MXenes follow the general formula of $M_{n+1}X_nT_x$ (n = 1–4), where (n + 1) number of "M" (the early transition metal layers) are interleaved by n number of "X" (carbon and/or nitrogen) atoms with abundant surface functionalities "T_x" (–F, –O, –OH). To date, more than 25 MXenes have been theoretically predicted, and approximately 14 have been experimentally realized.[25] Among these, $Ti_3C_2T_x$-the first and most extensively studied member, accounts for over 70% of all MXene-related publications.[26] Owing to its metallic conductivity, hydrophilic surface, and rich surface chemistry, $Ti_3C_2T_x$ has proven to be an exceptional electrode material for a variety of electrochemical applications, including supercapacitors, batteries, (photo)electrocatalysis, and sensing.[27] Moreover, recent studies have revealed the significant intrinsic electroactivity of $Ti_3C_2T_x$ in aqueous electrolytes, which is the most researched MXene to date.[28] In contrast to graphene or g-C_3N_4, but similar to transition metal dichalcogenides (TMDs) and black phosphorus (BP), $Ti_3C_2T_x$ MXenes exhibit irreversible redox behavior over a broad potential window.[29] It has been elucidated that the irreversible oxidation significantly passivates the $Ti_3C_2T_x$ MXene surface through the formation of TiO_2, and the extent of oxidation depends on the applied potential as well as the surrounding electrolyte. Notably, about 2.4% of the total Ti of a single $Ti_3C_2T_x$ particle is reported to be oxidized at an applied potential of 1.3 V for few-layered $Ti_3C_2T_x$ MXene particles validated using the single-particle impact method.[30] Despite these preliminary investigations on $Ti_3C_2T_x$ MXene's innate electrochemistry and the upsurge of interest in this new 2D family, a general literature survey finds a significant lack of understanding regarding their edge-specific electrochemistry. Akin to the previously discussed 2D materials, the Ti and C atoms at the $Ti_3C_2T_x$ MXene edge have a greater proclivity for unsaturated coordination than the basal plane owing to abrupt lattice termination. Thus, the atoms at the edges are likely to behave differently from the basal plane atoms, which is evident in many other 2D materials, revealing enhanced electrocatalytic activity and unique innate electrochemistry.[31] This provides an impetus to unravel whether similar activity exists at the $Ti_3C_2T_x$ MXene edge. Of particular interest are the innate electrochemical response, charge transfer kinetics, and catalytic activity at the edge of $Ti_3C_2T_x$ MXene compared to its basal counterpart.

In this work, we aim to provide experimental insights into the fundamental electrochemistry at the edge *vs.* basal plane of the $Ti_3C_2T_x$ MXene. This has been accomplished by fabricating high-quality free-standing $Ti_3C_2T_x$ MXene electrodes with defined edge and basal plane-oriented surfaces by developing a simple fabrication method, followed by selective surface passivation using insulating polymers. This method is unique and scalable for the mass production of edge-oriented $Ti_3C_2T_x$ MXene electrodes for a myriad of electrochemical applications. Characterization of the MXenes and the fabricated edge/basal plane electrodes was performed using X-ray diffraction (XRD), field electron scanning electron microscopy (FESEM), and Raman spectroscopy. The innate properties are studied and compared extensively under various commonly used electrolyte conditions. The HET rate of both basal and edge planes was investigated by using both the inner and the outer-sphere redox probes, namely $[Fe(CN)_6^{3-}]$, and $[Ru(NH_3)_6^{3+}]$. Finally, the electrocatalytic activities towards common analytes and the hydrogen evolution reaction (HER) are examined.

Results & discussion

$Ti_3C_2T_x$ MXene edge and basal plane electrode fabrication and characterization

The fabrication process for $Ti_3C_2T_x$ MXene edge- and basal-plane-oriented electrodes is exemplified in Fig. 1. First, we synthesized delaminated $Ti_3C_2T_x$ MXene flakes from parent Ti_3AlC_2 MAX phase by wet-chemical etching (Fig. 1a–c) according to the details described in the SI.[32] The dispersion containing delaminated 2D flakes was directly filtered through a membrane filtration system under vacuum (Fig. 1d). The filtrate was dried under vacuum at 100 °C for 2 hours to remove remnant solvent, and at this stage, we obtained a free-standing flexible MXene film (Fig. 1e). To obtain electrodes with the basal plane orientation, a simple selective surface passivation was done over the film surface using PDMS (Fig. 1f). The whole surface was first passivated for the edge electrode, followed by cutting across the film. This renders the exposed area containing maximum edge orientation selectively in the edge electrodes compared to the basal plane (Fig. 1g) and S1, SI. Of particular note is that the edge electrode was

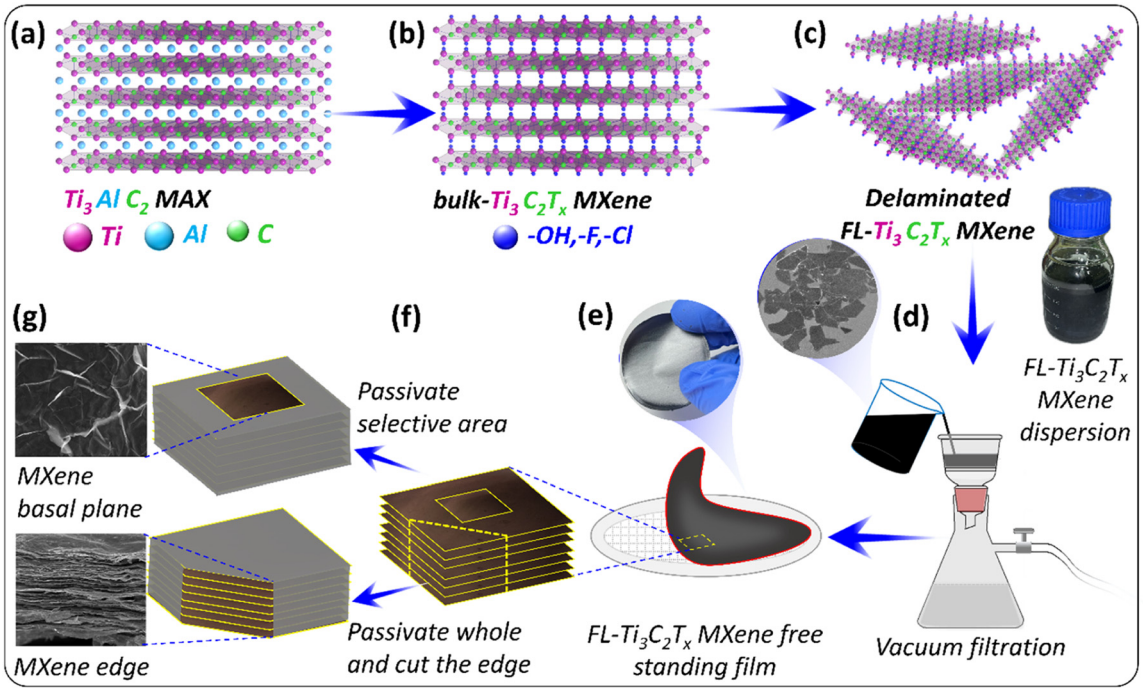

Fig. 1 Schematic of the exfoliation process for Ti_3AlC_2 and fabrication of $Ti_3C_2T_x$ MXene electrodes. (a) Ti_3AlC_2 MAX phase, (b) etching of Al layer and formation of bulk $Ti_3C_2T_x$, (c) delamination of bulk $Ti_3C_2T_x$ in to few-layer $Ti_3C_2T_x$ sheets, (d) vacuum filtration of FL-$Ti_3C_2T_x$ MXene dispersion to get $Ti_3C_2T_x$ free standing film (projection: FESEM image of $Ti_3C_2T_x$ flakes from the dispersion), (e) scheme and the digital image (projection) of the free-standing film, (f) selective surface passivation leading to edge and basal plane oriented electrodes, (g) FESEM image of the MXene edge and basal plane.

freshly cut across the film at all times before every electrochemical measurement, keeping the sensitivity of unsaturated atoms at the edge in mind.

The above-discussed fabrication procedure specifically allows ordered sheet stacking, enabling edge orientation in the horizontal direction, as confirmed by FESEM in Fig. 2a. The orientation of edge plane sites is visible in the high-resolution cross-sectional FESEM image in Fig. 2b. In contrast, the basal plane surface of the film (Fig. 2c and d) primarily contains flat lands of MXene with comparatively fewer edges contributed by individual flakes. The film thickness can readily be controlled by controlling the concentration of flake dispersion during the filtration process. The average thickness was found to be 52 ± 3 μm (Fig. S2) from 50 ml of as-prepared MXene dispersion from a typical synthesis procedure discussed in the SI. The successful etching of Ti_3AlC_2 MAX to $Ti_3C_2T_x$ MXene was confirmed by XRD presented in Fig. 2e.[24,25] The typical peaks corresponding to the MAX phase are absent in the MXene free-standing film, confirming the successful etching of Al from the MAX lattice. Here, the signature peak (002) shifts from $2\theta = 9°$ to a lower angle at $2\theta = 7°$ concomitantly with a substantial increase in FWHM, indicative of enhancement in interlayer spacing in the free-standing film. The enhanced interlayer spacing is validated from the cross-sectional FESEM image shown in Fig. 2b.

Raman spectroscopy is a powerful tool to probe vibrational modes, providing molecular-level insight into bonding, strain, defects, and functionalization – all of which differ between edge and basal regions. The variation in molecular structure at the edge plane electrodes compared to the basal plane was investigated by Raman spectroscopy. Fig. 2f shows the Raman spectra recorded from 100 cm^{-1} to 1800 cm^{-1} at room temperature from the $Ti_3C_2T_x$ MXene film, focusing on both the top surface of the film (basal plane) and the freshly cut edge of the film (edge plane). The Raman spectra of MXenes generally comprise two spectral regions, one in the low-frequency (100–800 cm^{-1}) region (Fig. 2g and h) representing the lattice vibrations (phonons), and higher frequency ones (1000–1800 cm^{-1}) representing the C–C stretching vibrations occurring in MXene (Fig. 3i).[33] The low-frequency region consists of two representative modes, namely, E_g (Ti, C, O) and A_{1g} (Ti, C, O), representing the in-plane and out-of-plane vibrations of titanium atoms, carbon atoms, and surface groups, respectively. Along with the resonant peak at 123 cm^{-1}, two distinct sharp peaks appear at 205 cm^{-1} and 734 cm^{-1}, representative of A_{1g} (Ti, O, C) and A_{1g} (C) vibrational modes, respectively (red peaks in Fig. 2g and h). The rest of the region typically is the fingerprint of surface groups that split into two representative regions, namely, the regions 230–470 cm^{-1} (Fig. 2g) and 580–730 cm^{-1} (Fig. 2h), which represent the in-plane (E_g) vibration of surface groups attached to Ti atoms and the C atoms, respectively. While comparing the peaks at the edge *vs.* basal planes, we observed that no shift occurs for the resonant peak at 123 cm^{-1} and the A_{1g} (Ti, O, C) at

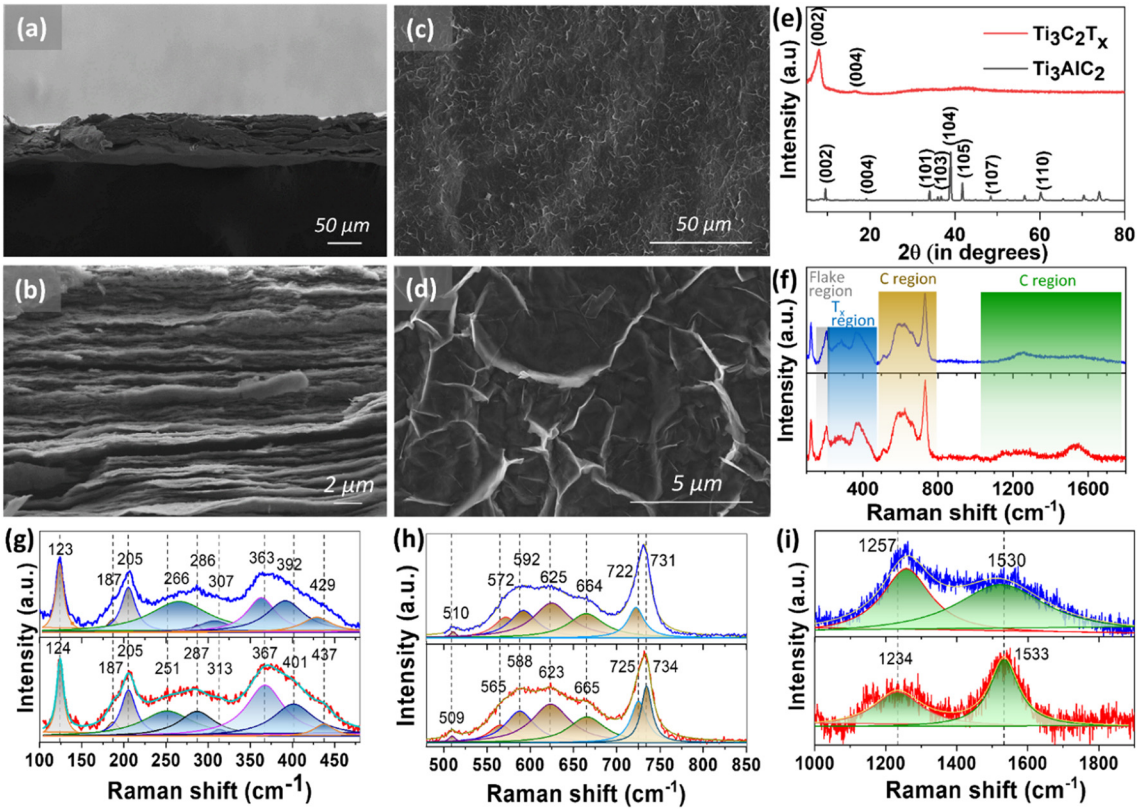

Fig. 2 Characterization of the fabricated basal & edge plane $Ti_3C_2T_x$ MXene film electrodes: FESEM image of (a and b) $Ti_3C_2T_x$ MXene edge plane and (c and d) basal plane electrodes at different magnifications. (e) XRD patterns of Ti_3AlC_2 MAX phase & the synthesized $Ti_3C_2T_x$ MXene film. (f) Comparison of the full Raman spectra recorded over MXene basal plane (plot) & edges (blue plot). (g–i) A detailed comparison of deconvoluted spectra in different frequency regions respectively.

205 cm^{-1}. Enhanced disorder at edges leads to peak broadening and/or shifting due to more diverse bonding environments. The disorder-related vibrational modes imply local states that may facilitate faster charge transport. However, a mild red shift (734 cm^{-1} to 731 cm^{-1}) occurs for A_{1g} (C) vibrational modes for the edge compared to the basal planes, which is attributed to the larger edge density in edge electrodes compared to the basal planes.[34] In the Ti–T_x region (230–470 cm^{-1}), the peak at 252 cm^{-1} blue shifts to 266 cm^{-1}, indicative of a lack of terminal groups at the freshly cut edge plane compared to the basal plane.[35] As reported, the vibration of the surface terminal groups weakens the out-of-plane motion of surface Ti_2, whereas it strengthens the out-of-plane vibration of C atoms.[36] However, no major peak shifts are seen in the deconvoluted peaks. Further detailed studies need to be done to understand the impact of unsaturated C and Ti of the edge plane in the Raman fingerprint spectra of MXene.

The last key region exclusively representing the C–C stretching vibrations is at the higher frequency end (1000–1800 cm^{-1}). This region consists of the G-band, appearing from C–C bond vibration in all SP^2 hybridized carbons, while the D-band originates from the disordered carbons in the MXene lattice. As observed, the D-band for basal plane MXene shifts from 1232 cm^{-1} to 1257 cm^{-1}, along with peak broadening, and is fairly stronger for edge plane MXene electrodes. This is attributed to a larger number of defects in the edge plane compared to the basal plane.[37] In contrast, the G-band shifts from 1534–1530 cm^{-1} while going from the basal plane to the edge with substantial peak width broadening, which indicates the presence of disordered C in the edge.[38] This undoubtedly validates that edge electrodes consist of more disordered atoms compared to the basal plane.

Inherent electrochemistry of edge *vs.* basal plane $Ti_3C_2T_x$ MXene electrodes

Despite extensive use of $Ti_3C_2T_x$ MXene in electrochemical applications, understanding its stability when used as an electrode is inadequate. It is exciting to explore the stability and the electrochemical working window at the electroactive edge plane compared to the basal plane sites. We conduct cyclic voltammetry for both edge and basal plane electrodes in six different commonly used electrolytes over a wide potential window, preferably lower than the potential at which hydrogen evolution and water oxidation occur. Each time, several consecutive scans were recorded to understand the electroactivity of the electrodes on repeated use. To identify the repeatability, we also performed each experiment

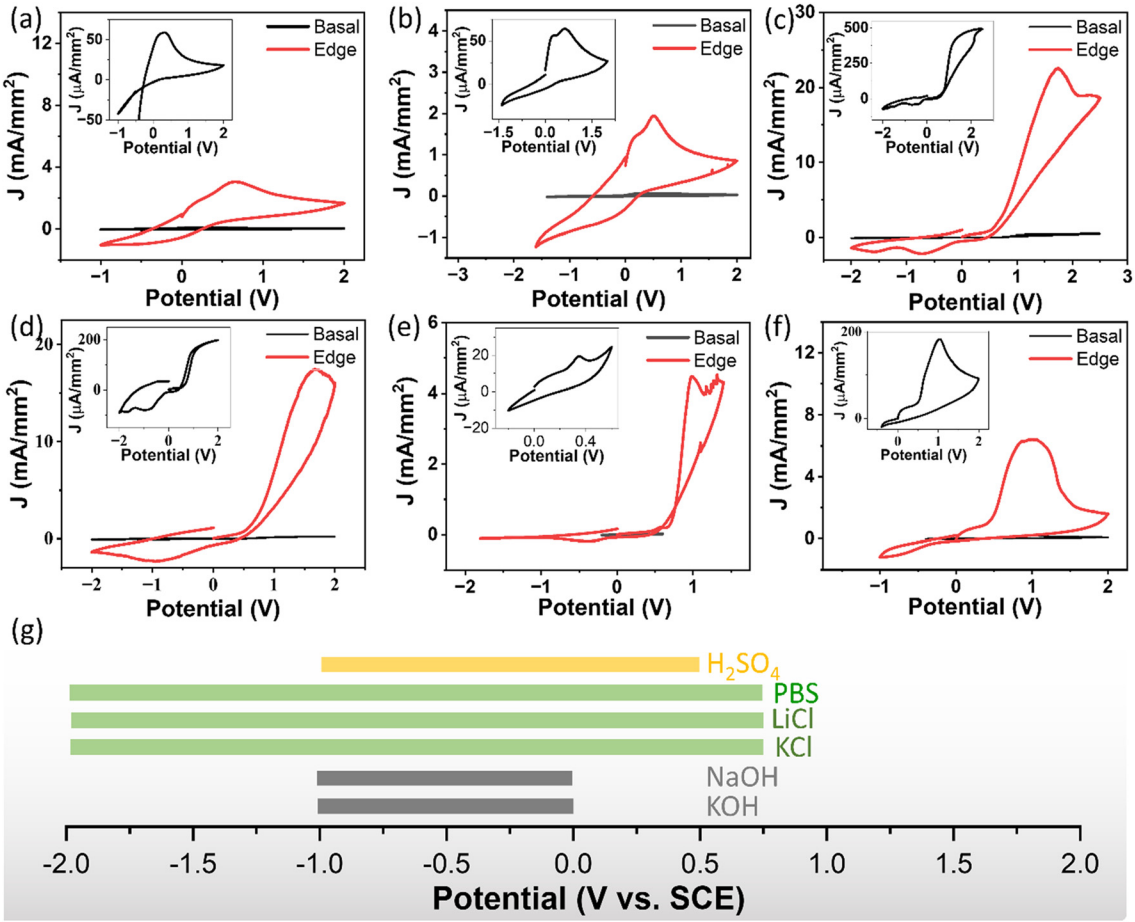

Fig. 3 Cyclic voltammograms of edge & basal $Ti_3C_2T_x$ film electrodes in (a) 0.1 M KOH, (b) 0.1 M NaOH, (c) 0.1 M KCl, (d) 0.1 M LiCl, (e) 0.01 M phosphate buffered saline (PBS), and (f) 0.1 M H_2SO_4. (g) Electrochemical potential window for edge electrodes in various electrolyte conditions. All the measurements were performed relative to an external saturated calomel reference electrode (SCE) at the scan rate of 50 mV s^{-1} under thermostatic conditions (temperature: 25 °C). Insets show the zoomed CV responses of the basal-plane electrode.

multiple times under the same experimental conditions. Fig. 3 depicts the voltammetric profile for both edge (red) and basal plane (black) electrodes in 0.1 M KOH, NaOH, KCl, LiCl, 0.01 M PBS (pH 7), and 0.1 M H_2SO_4, respectively. As observed in Fig. 3a, the first scan results in a broad oxidation peak at *ca.* 0.66 V for the edge plane electrode and 0.31 V for the basal-plane electrode in KOH. However, a significantly intense oxidation current (~47 times) is observed for the edge plane electrode compared to the basal plane electrodes. It is seen that the oxidation current decreases slowly in the subsequent scans for the edge plane electrode; however, a sharp decrease in current is observed for the basal counterparts, as seen in Fig. S3a and d. Large oxidation current density at the edge and its slow decrease in subsequent scans point to the possibility of abundant oxidizable moieties at edge-plane sites compared to the basal plane. Also, the background capacitance in both negative and positive potential ranges is low and stable, as observed in Fig. S3. No prominent inherent peaks are observed in the reduction end for both edge and basal plane electrodes, suggesting a stable potential window in the negative potential range (−1 V to 0 V) for KOH medium. Also, as illustrated in Fig. S3, not much deviation is observed in the current profile in three repeated measurements for both edge and basal plane electrodes (Fig. S3a–f). The area of the basal electrodes is shown in Fig. S3g–i. A very similar trend is observed in NaOH electrolyte medium as illustrated in Fig. 3b and S4, SI. However, the oxidation peak for KCl (Fig. 3c and S5) shifts towards higher potential, *ca.* 1.7 V for edge plane electrodes, and *ca.* 1.6 V for basal plane electrodes. The average current density is about ~53 times higher in edge plane electrodes compared to basal planes. In addition, the capacitive background current is merged with mild and stable redox peaks at −0.7 V and −1.5 V, respectively. This squeezes the potential window from −0.5 V to 1 V. Similar features are observed for neutral electrolytes such as LiCl (Fig. 3d and S6) and PBS (Fig. 3e and S7), where the working potential window was found to be in the range from −2 V to ~0.7 V for the edge electrodes with mild and stable redox peaks in the negative window. The inference drawn from this comparatively wide potential window found in a neutral electrolyte medium depicts the prospective use of edge plane electrodes in various applications in neutral media, where the interference due to innate oxidation is presumed to be minimal. In acidic

electrolyte (H_2SO_4, Fig. 3f and S8), the oxidation potential is at *ca.* 1 V at both the edge and basal plane, with an oxidation current density ~30 times higher at the edge than the basal plane. The working potential window appears to be from −1.0 V to 0.5 V with apparently low and stable background capacitance, suggestive of the usability of these electrodes in the allowed potential window. The allowed potential windows for different electrolyte conditions at the $Ti_3C_2T_x$ MXene edge are shown in Fig. 3g. These findings explored strikingly boosted innate electroactivity at the MXene edge, compared to the basal plane, and its limited working potential window in various commonly used electrolyte media. These unique oxidative properties are inherent to MXene and are irreversible. They originate from the oxidation of unsaturated Ti in the $Ti_3C_2T_x$ lattice, presumably at the defect sites. The as-prepared MXenes often contain surface defects due to their harsh acidic synthesis medium, which creates moieties (unsaturated Ti) prone to oxidation in the MXene lattice.[39,40] However, the discontinuity at the freshly cut edge plane enables a greater propensity of unsaturated coordination compared to the basal plane, resulting in more oxidation compared to its basal counterpart. In addition, the oxidation rate seems fast in an acidic medium, leaving a substantially decreased oxidation current in the 2nd scan. In contrast, a gradual decrease in oxidation current is observed in subsequent scans in neutral and alkaline media. Further in-depth studies are needed to unveil these redox mechanisms. As the catalytic activity of the 2D materials depends on the density of edge sites, it becomes crucial to optimize the edge structure to boost the performance. This study provides a guideline on applying MXene in selective application areas where its innate oxidation will not impede the electrochemistry of interest.

The electron transfer mechanism and the heterogeneous electron transfer rate (HET) at the MXene edge, compared to basal plane electrodes, were investigated with the aid of both inner ($[(Fe(CN)_6)]^{3-/4-}$) and outer sphere ($[Ru(NH_3)_6]^{3+/2+}$) redox probes. It is worth mentioning that the redox mechanism in $[(Fe(CN)_6)]^{3-/4-}$ is surface sensitive; however, $[Ru(NH_3)_6]^{3+/2+}$ does not depend on electrode surface structure. We conducted controlled experiments by conducting measurements over three different electrodes for each set of measurements. For $[(Fe(CN)_6)]^{3-/4-}$, the basal plane electrodes manifested well-defined redox peaks at low scan rates (Fig. 4a and S9 SI) with $\Delta E_p^{basal} \approx 115$ mV and corresponding heterogeneous charge transfer rate $k^0_{obs} = 1.16 \times 10^{-3}$ cm s^{-1}, calculated using Nicholson's analysis.[41] However, the redox peak is significantly superimposed by the capacitive current for edge plane electrodes, showing barely visible redox peaks corresponding to $\Delta E_p^{edge} \approx 90$ mV ($k^0_{obs} = 2.38 \times 10^{-3}$ cm s^{-1}). No other clear redox peaks are observed in the CV, indicating a nominal impact of the most plausible inherent oxidative current for $[Fe(CN)_6]^{3-/4-}$. The most convincing explanation is the large potential window of MXene in a KCl electrolyte medium (Fig. 3c). Thus, the edge plane electrode is much active than the basal plane electrode, exhibiting about 2.3 times faster HET rate at a low scan rate. However, the large capacitive current at the edge-rich MXene electrodes impedes the determination of the ΔE_p value at other scan rates. In contrast to the above findings for $[Fe(CN)_6]^{3-/4-}$, the redox reaction for $[Ru(NH_3)_6]^{3+/2+}$ redox probes exhibited well-defined redox peaks at various scan rates (Fig. 4b and S10), most plausibly as the redox window (−0.5 to 0.2 V) is far apart from the innate oxidation potential of MXenes (~1.5 V). Notably, the basal plane MXene electrode exhibits prominent redox peaks with less capacitive current compared to the edge plane electrode, showcasing about ~36 times elevated current density at the edge. Also, the peak-to-peak separation (ΔE_p) is observed at $\Delta E_p^{basal} \approx 119$ mV for the basal plane and $\Delta E_p^{edge} \approx 107$ mV for the edge electrode, validating that the edges are more active compared to the basal plane. Based on these ΔE_p values at different scan rates (Fig. S10, SI), the calculated HET rate for the edge was found to be $(18.5 \pm 0.6) \times 10^{-4}$ cm s^{-1}, which is about ~2.1 times faster compared to the basal plane $(8.76 \pm 0.43) \times 10^{-4}$ cm s^{-1} (Fig. S11, SI).

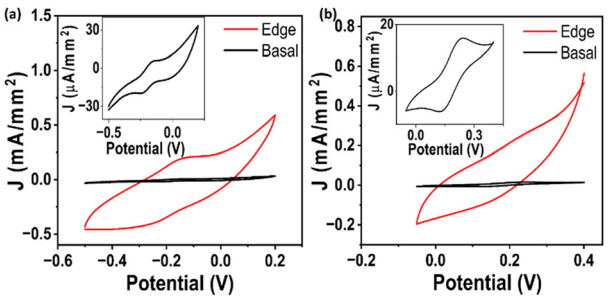

Fig. 4 Cyclic voltammograms for the edge & basal $Ti_3C_2T_x$ film electrodes in 0.1 M KCl supporting electrolyte containing (a) 20 mM $K_4Fe(CN)_6{\cdot}3H_2O$ & (b) 20 mM $[Ru(NH_3)_6]Cl_3$ redox probes. All the measurements were performed relative to an external saturated calomel reference electrode (SCE) at the scan rate of 50 mV s^{-1} under thermostatic conditions (temperature: 25 °C ± 1 °C). Insets shows the zoomed CV responses of the basal-plane electrode.

Complementing the findings on faster HET rates at the edge plane electrodes compared to their basal counterparts, we evaluated the catalytic activity of both the edge and basal plane MXene electrodes towards two biologically important compounds (*i.e.*, dopamine and ascorbic acid), as well as the hydrogen evolution reaction. As depicted in Fig. 5a and b, a considerably higher sensitivity is observed at the edge plane electrodes compared to the basal planes. Notably, the faradaic current due to dopamine oxidation is 4.4 times larger at the edge than at the basal plane. Furthermore, the oxidation potential is significantly lower (0.13 V) at the edge plane MXene electrodes than at the basal plane (0.33 V), showcasing much higher sensitivity at the edge. A similar trend is seen with ascorbic acid, where the oxidation current is 3.9 times greater at the edge in comparison to the basal plane. These findings suggest that the MXene edge plane is more catalytically active towards biologically significant molecules than the basal planes.

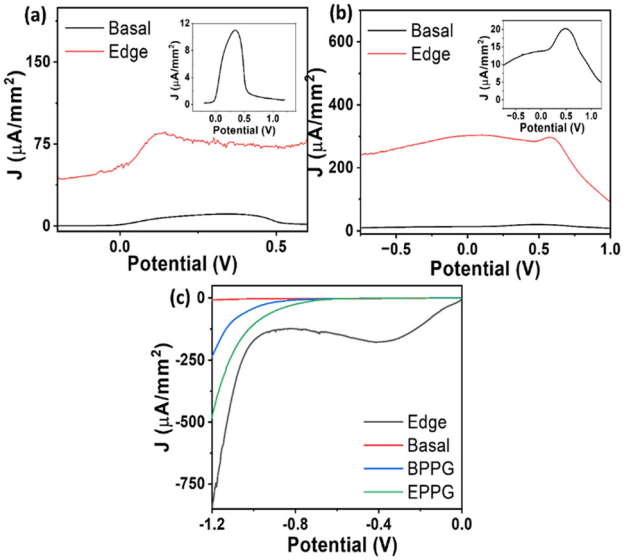

Fig. 5 Differential pulse voltammetry (DPV) of the edge & basal $Ti_3C_2T_x$ film electrodes in 0.01 M phosphate buffered saline (PBS) supporting electrolyte containing (a) 20 mM ascorbic acid and (b) 20 mM dopamine. (c) Linear sweep voltammetry (LSV) represents the HER performance study of the edge & basal $Ti_3C_2T_x$ film electrodes compared with commercial EPPG and BPPG electrodes in 0.1 M H_2SO_4 electrolyte. All the electrochemical measurements were performed relative to an external saturated calomel reference electrode (SCE) at the scan rate of 50 mV s^{-1}, and LSV measurements were performed at 5 mV s^{-1} under thermostatic conditions (temperature: 25 °C ± 1 °C). Insets in (a) and (b) show the zoomed LSV responses of the basal-plane electrode.

Research into the HER activity of $Ti_3C_2T_x$ MXene has garnered significant attention in recent years. While surface engineering with catalyst particles has dramatically enhanced catalytic activity, bare $Ti_3C_2T_x$ MXene is often found to be less catalytically active toward H_2 evolution. However, the catalytic H_2 evolution at the edge of $Ti_3C_2T_x$ MXene remains unexplored. Our findings on the high HET rate and sensitivity at the MXene edge plane encourage us to investigate the catalytic HER activity at the edge compared to its basal counterpart. Electrochemical measurements were performed directly in a 0.1 M H_2SO_4 solution to investigate their HER activities. Fig. 5c depicts the HER polarization plot for the MXene edge plane and the basal plane electrodes at a sweep rate of 5 mV s^{-1}. The same experiments were repeated for three different edge plane electrodes, which are shown in Fig. S12, SI. For comparison, we also recorded the HER activities at the commercial basal plane pyrolytic graphite (BPPG) and edge plane pyrolytic graphite electrode (EPPG). As observed, a very small current response exhibiting negligible HER activity is seen for the basal plane $Ti_3C_2T_x$ MXene electrode. In contrast, the edge plane electrode shows enhanced HER activity, exemplified by high current density and low onset potential. Notably, a current density of −170 μA mm^{-2} is observed for edge plane electrodes at an onset potential of −1 V, which is 55 times larger than the basal plane MXene (−3 μA mm^{-2}) electrode and 1.2 times larger than the commercial EPPG (−140 μA mm^{-2}) and about 4 times larger than commercial BPPG (−41 μA mm^{-2}) electrode. It is worth noting that the commercial edge plane graphite also exhibits larger HER activity compared to its basal plane counterpart. The larger current density in edge electrodes confirms the enrichment effect of active edge sites of $Ti_3C_2T_x$ MXene, suggestive of superior catalytic activity of edges compared to the basal planes, aligning with the general trend in nature for layered materials.

Conclusions

We propose a straightforward method for fabricating edge-plane-oriented $Ti_3C_2T_x$ MXene electrodes and systematically investigate their inherent electrochemical behaviour, charge transfer, and catalytic activities in comparison to their basal plane counterparts. Our results reveal that the inherent electrochemistry is significantly more pronounced at the edge sites than at the basal regions across a variety of commonly used electrolyte media. The observed irreversible oxidation significantly limits the working potential window and is visibly wider for neutral electrolytes compared to both acidic and alkaline media. Such limitations directly impact the applicability of $Ti_3C_2T_x$ MXenes in sensing analytes with redox potentials that lie beyond these constrained potential windows. Furthermore, the edges exhibited an enhanced HET rate compared to the basal planes for the outer-sphere redox probe. However, the intrinsic oxidation substantially inhibits the calculation of the HET rate for the inner-sphere redox probe. Additionally, the edge electrodes demonstrated superior catalytic activity towards important biologically relevant molecules when compared to the basal plane. This trend of enhanced electrochemical activity at the edge plane was further substantiated by the HER studies, validating the hypothesis that edges are more active than the basal plane for the 2D materials. This fundamental investigation represents the first-ever study on the electrochemistry of MXene edges over the basal plane of MXene that will guide the future design and application of $Ti_3C_2T_x$ MXenes in electrocatalysis and electrochemical sensing.

Author contributions

Shubham B. Upadhye: conceptualization, methodology, experimental data acquisition, investigation, writing – original draft. Gopal K. Pradhan: formal analysis, investigation. Pranati Nayak: conceptualization, writing – review & editing, supervision, funding acquisition.

Conflicts of interest

There are no conflicts to declare.

Data availability

The authors declare that the data supporting this manuscript's findings can be found in the supplementary

information (SI). The raw data is available from the corresponding author upon request.

Supplementary information is available. See DOI: https://doi.org/10.1039/d5lf00354g.

Acknowledgements

The research reported in this manuscript is supported by funding from the Anusandhan National Research Foundation (ANRF), Government of India, through the Ramanujan Grant (Grant No. RJF/2021/000110). PN thanks ANRF for awarding the Prime Minister Early Career grant (ANRF/ECRG/004898/PMS). The authors would like to thank the Central Characterization Facility, ICT, and IOCB for various characterizations. G. K. P. acknowledges the use of the Micro-Raman facility at the central research facility (CRF) of KIIT Deemed to be University, Bhubaneswar.

References

1 W. Yuan, Y. Zhou and Y. Li, *et al.*, *Sci. Rep.*, 2013, **3**, 2248.
2 H. I. Karunadasa, *et al.*, *Science*, 2012, **335**, 698–702.
3 A. N. Patel, M. G. Collignon, M. A. O'Connell, W. O. Y. Hung, K. McKelvey, J. V. Macpherson and P. R. Unwin, *J. Am. Chem. Soc.*, 2012, **134**, 20117–20130.
4 X. Zhang, J. Xin and F. Ding, *Nanoscale*, 2013, **5**, 2556–2569.
5 J. Kibsgaard, Z. Chen and B. Reinecke, *et al.*, *Nat. Mater.*, 2012, **11**, 963–969.
6 A. Bellunato, H. Arjmandi Tash, Y. Cesa and G. F. Schneider, *ChemPhysChem*, 2016, **17**, 785.
7 M. Velický, P. S. Toth, C. R. Woods, K. S. Novoselov and R. A. W. Dryfe, *J. Phys. Chem. C*, 2019, **123**, 11677–11685.
8 A. Ambrosi, C. K. Chua, N. Mohamad Latiff, A. H. Loo, C. H. A. Wong, A. Y. S. Eng, A. Bonanni and M. Pumera, *Chem. Soc. Rev.*, 2016, **45**, 2458–2493.
9 A. Ambrosi and M. Pumera, *Chem. – Eur. J.*, 2013, **19**, 4748–4753.
10 G. R. Bhimanapati, Z. Lin, V. Meunier, Y. Jung, J. Cha, S. Das, D. Xiao, Y. Son, M. S. Strano, V. R. Cooper, L. Liang, S. G. Louie, E. Ringe, W. Zhou, S. S. Kim, R. R. Naik, B. G. Sumpter, H. Terrones, F. Xia, Y. Wang, J. Zhu, D. Akinwande, N. Alem, J. A. Schuller, R. E. Schaak, M. Terrones and J. A. Robinson, *ACS Nano*, 2015, **9**, 11509–11539.
11 X. Chia and M. Pumera, *Nat. Catal.*, 2018, **1**, 909–921.
12 Y. T. Yew, C. S. Lim, A. Y. S. Eng, J. Oh, S. Park and M. Pumera, *ChemPhysChem*, 2016, **17**, 481.
13 M. Z. Mohamad Nasir, Z. Sofer, A. Ambrosi and M. Pumera, *Nanoscale*, 2015, **7**, 3126–3129.
14 X. Chia, A. Ambrosi, Z. Sofer, J. Luxa and M. Pumera, *ACS Nano*, 2015, **9**, 5164–5179.
15 A. Y. S. Eng, A. Ambrosi, Z. Sofer, P. Šimek and M. Pumera, *ACS Nano*, 2014, **8**, 12185–12198.
16 S. M. Tan, A. Ambrosi, Z. Sofer, Š. Huber, D. Sedmidubský and M. Pumera, *Chem. – Eur. J.*, 2015, **21**, 7170–7178.
17 H. Yu, X. Yu, Y. Chen, S. Zhang, P. Gao and C. Li, *Nanoscale*, 2015, **7**, 8731–8738.
18 H. I. Karunadasa, E. Montalvo, Y. Sun, M. Majda, J. R. Long and C. J. Chang, *Science*, 2012, **335**, 698–702.
19 J. Kibsgaard, Z. Chen, B. N. Reinecke and T. F. Jaramillo, *Nat. Mater.*, 2012, **11**, 963–969.
20 J. Xie, H. Zhang, S. Li, R. Wang, X. Sun, M. Zhou, J. Zhou, X. W. Lou and Y. Xie, *Adv. Mater.*, 2013, **25**, 5807–5813.
21 J. Luxa, P. Vosecký, V. Mazánek, D. Sedmidubský, M. Pumera, P. Lazar and Z. Sofer, *ACS Catal.*, 2017, **7**, 5706–5716.
22 P. Marvan, Š. Huber, J. Luxa, V. Mazánek, D. Sedmidubský, Z. Sofer and M. Pumera, *Appl. Mater. Today*, 2019, **16**, 179–184.
23 L. Wang, Z. Sofer and M. Pumera, *ChemElectroChem*, 2015, **2**, 324–327.
24 Z. Sofer, D. Sedmidubský, Š. Huber, J. Luxa, D. Bouša, C. Boothroyd and M. Pumera, *Angew. Chem., Int. Ed.*, 2016, **55**, 3382.
25 M. Naguib, M. Kurtoglu, V. Presser, J. Lu, J. Niu, M. Heon, L. Hultman, Y. Gogotsi and M. W. Barsoum, *Adv. Mater.*, 2011, **23**, 4248–4253.
26 M. Naguib, O. Mashtalir, J. Carle, V. Presser, J. Lu, L. Hultman, Y. Gogotsi and M. W. Barsoum, *ACS Nano*, 2012, **6**, 1322–1331.
27 M. Naguib, V. N. Mochalin, M. W. Barsoum and Y. Gogotsi, *Adv. Mater.*, 2014, **26**, 992–1005.
28 B. Xu and Y. Gogotsi, *Adv. Funct. Mater.*, 2020, **30**, 2007011.
29 J. Tang, T. S. Mathis, N. Kurra, A. Sarycheva, X. Xiao, M. N. Hedhili, Q. Jiang, H. N. Alshareef, B. Xu, F. Pan and Y. Gogotsi, *Angew. Chem., Int. Ed.*, 2019, **58**, 17849.
30 P. Nayak, Q. Jiang, R. Mohanraman, D. Anjum, M. N. Hedhili and H. N. Alshareef, *Nanoscale*, 2018, **10**, 17030–17037.
31 P. Nayak, M. Yang, Z. Wang, X. Li, R. Miao and R. G. Compton, *Appl. Mater. Today*, 2022, **26**, 101335.
32 A. N. Patel, M. G. Collignon, M. A. O'Connell, W. O. Y. Hung, K. McKelvey, J. V. Macpherson and P. R. Unwin, *J. Am. Chem. Soc.*, 2012, **134**, 20117–20130.
33 M. Alhabeb, K. Maleski, B. Anasori, P. Lelyukh, L. Clark, S. Sin and Y. Gogotsi, *Chem. Mater.*, 2017, **29**, 7633–7644.
34 S. Adomaviciute-Grabusove, A. Popov, S. Ramanavicius, V. Sablinskas, K. Shevchuk, O. Gogotsi, I. Baginskiy, Y. Gogotsi and A. Ramanavicius, *ACS Nano*, 2024, **18**, 13184–13195.
35 A. Sarycheva, M. Shanmugasundaram, A. Krayev and Y. Gogotsi, *ACS Nano*, 2022, **16**, 6858–6865.
36 A. Sarycheva and Y. Gogotsi, *Chem. Mater.*, 2020, **32**, 3480–3488.
37 A. K. Gupta, T. J. Russin, H. R. Gutiérrez and P. C. Eklund, *ACS Nano*, 2009, **3**, 45–52.
38 C. Casiraghi, A. Hartschuh, H. Qian, S. Piscanec, C. Georgi, A. Fasoli, K. S. Novoselov, D. M. Basko and A. C. Ferrari, *Nano Lett.*, 2009, **9**, 1433–1441.
39 V. Natu, M. Sokol, L. Verger and M. W. Barsoum, *J. Phys. Chem. C*, 2018, **122**, 27745–27753.
40 V. Natu, J. L. Hart, M. Sokol, H. Chiang, M. L. Taheri and M. W. Barsoum, *Angew. Chem., Int. Ed.*, 2019, **58**, 12655–12660.
41 R. S. Nicholson, *Anal. Chem.*, 1965, **37**, 1351–1355.